Lateral energy transport in laser-produced plasmas

D. Vick,[1] M. Kado,[2] H. Yamamoto,[2] K. A. Tanaka,[3] A. A. Offenberger,[1] C. E. Capjack,[1] A. Nishiguchi,[2] K. Mima,[2] and S. Nakai[2]

[1]*Department of Electrical Engineering, University of Alberta, Edmonton, Alberta, Canada T6G 2G7*

[2]*Institute of Laser Engineering, Osaka University, Yamada-oka 2-6, Suita, Osaka 565, Japan*

[3]*Department of Electromagnetic Energy Engineering, Osaka University, Yamada-oka 2-1, Suita, Osaka 565, Japan*

(Received 12 December 1994)

Lateral energy transport in laser-produced plasmas has been studied by irradiating planar polystyrene foils with 0.53-μm-wavelength, spatially nonuniform laser beams. Spatially resolved x-ray emission patterns and spectra were recorded to infer the temperatures, ionization states, and time-integrated hydrodynamic histories of plasma originating from tracer layers embedded in the targets. The conditions of the experiment have been simulated using a two-dimensional single fluid hydrodynamic code. The experimental results and code predictions are in good agreement, indicating that a moderate amount of ablation occurs in the nonirradiated region of the target.

PACS number(s): 52.25.Fi, 52.25.Nr, 52.50.Jm, 52.65.Rr

I. INTRODUCTION

The success of a number of proposed applications for laser-produced plasmas, such as direct drive inertial confinement fusion and x-ray lasers, requires spatial uniformity in the energy coupling between the laser and the ablating targets. The formation of hydrodynamic structures in the blowoff plasma due to nonuniformities in the incident laser (whether inherent or artificially imposed) and the influence of such structures on energy transport are therefore of interest to the laser plasma community. Electron thermal conduction has been thought to play a central role in smoothing away such nonuniformity between the laser absorption and ablation surfaces. As a first approximation to this effect the steady state cloudy day model [1] predicts that lateral ablation pressure nonuniformities of spatial wave number k will be damped by the factor $\exp(-kD)$, where the standoff distance D represents the separation between the laser absorption and ablation surface. Manheimer, Colombant, and Gardner presented a somewhat enhanced model [2] (henceforth termed the MCG model) in which the linearized fluid equations were solved self-consistently with classical thermal conduction under the assumption of near-one-dimensional flow with weak lateral perturbations. In this model hydrodynamic pressure perturbations produce an additional smoothing factor of approximately $\exp(-1.34kD)$.

A number of experimental studies aimed at characterizing the thermal smoothing process have relied on rear-side measurements of the velocity of planar foils accelerated by spatially modulated laser beams. In early work, conducted by Obenschain and co-workers using 1.05-μm laser light at intensities up to 10^{14} W/cm^2 [3], ablation uniformity as inferred from Doppler shift or impact foil techniques was reported to increase with laser intensity. Later x-ray shadowgraphy measurements [4,5] of the rear side of foils illuminated by 1.05-, 0.53-, and 0.35-μm lasers have indicated a progressive reduction in smoothing with decreasing laser wavelength. Such results are in accordance with one-dimensional steady state models [2,6] that predict the standoff distance to scale as $I_{\rm abs}^{4/3}\lambda^{14/3}$. More recently, temporally and spatially resolved optical measurements of the shock breakout at the rear of nonuniformly irradiated foils have been performed, which indicate significant smoothing of 0.53-μm light at intensities above 5×10^{13} W/cm^2 [7]. The highest spatial resolution yet achieved in such experiments (1 μm) suggests the degree of smoothing to lie between the predictions of the cloudy day and the MCG models [8].

A limited amount of complementary work, relying mainly on x-ray diagnostics, has been done to characterize lateral transport at the ablation sides of targets. In one experiment in which spatially modulated 0.27-μm light was focused onto plastic-coated aluminum targets, profiles from x-ray pinhole images revealed no evidence of widening of the ablation front [9]. Two-dimensional high-resolution x-ray images indicate that even in beams optically smoothed by induced spatial incoherence techniques, small scale illumination nonuniformities present during the very early times can create persistent structures at the ablation front, which remain for the duration of the pulse [10]. These measurements call into question the efficiency of the thermal smoothing process. In addition to these studies, a number of experiments undertaken with single unmodulated beams have addressed energy transport into the target substrate beyond the laser focus. Observed differences in the intensity scaling of mass ablation rates as inferred from ion versus x-ray diagnostics have been attributed to the existence of a region of ablation outside the focal spot [11,12]. However, broadband x-ray microscope images of the focal spot have revealed little evidence of lateral heating of the target for the laser wavelengths of 1.05 and 0.53 μm and intensities of 10^{14} W/cm^2 [13]. At somewhat higher intensities of

$(0.5-1)\times W/cm^2$, pinhole images from aluminum planar targets have revealed soft-x-ray emission features adjacent to the target surface that extend as much as 100 μm beyond the focal spot; these features may be due to heating of the substrate by suprathermal electrons [14]. Recently, time-resolved x-ray images of exploding titanium foils have revealed ring-shaped heat fronts with radial expansion velocities indicative of thermal flux inhibition [15].

In this paper we describe a set of measurements aimed at assessing the effect of lateral transport by using the spatially resolved signature of x-ray emission from multilayer planar targets. Two focal spot conditions were used in order to assess lateral energy transport directed (1) outward from the edge of a single laser spot and (2) between two hot spots of a nonuniformly irradiated target. In parallel with the experiments, a number of simulations were conducted on a two-dimensional hydrodynamic code. The code was capable of simulating multilayer targets and included an atomic physics package that allowed numerically generated x-ray emissivity patterns to be compared with experimental images.

II. EXPERIMENTAL DETAILS

The experiments were conducted using the GEKKO IV neodymium glass laser at the Institute of Laser Engineering of Osaka University. Shaped pulses with a Gaussian temporal profile and a nominal full width at half maximum (FWHM) of 860 or 400 ps were frequency doubled by a type-II potassium dihydrogen phosphate (KDP) crystal and focused at normal incidence onto planar polystyrene (CH) targets of thickness 15–18 μm. The pulse selector and isolation units in the early stages of the laser limited the prepulse level to less than 2×10^{-6} times that of the main pulse. An infrared-absorbing filter positioned after the KDP crystal attenuated the unconverted 1.05-μm light by a factor of approximately 10^5.

For the first of two focal conditions, nonuniform irradiation conditions on target were created by inserting a mask of parallel opaque strips into the beam and positioning the target to lie on the convergent side of best focus. The resulting focal spot consisted of alternating regions of high and low intensity of equal width (56 μm), superimposed within a nominal focal spot diameter of 300 μm, with most of the laser energy deposited in two strips situated on either side of the laser axis. The peak intensities for this focal condition ranged from 3×10^{12} to 3×10^{13} W/cm^2. For the second focal condition the target was positioned to produce the tightest possible focal spot resulting in intensities of up to 3×10^{14} W/cm^2 within a 110-μm-diam spot.

The targets consisted of polystyrene foils onto which single signature layers of aluminum (Al) or double layers of sodium fluoride (NaF) over aluminum were vacuum deposited. The layers were of thickness 0.1 μm and were buried under an additional CH overcoat of thickness varying from 0 to 1.2 μm. By using such targets it was possible to record x-ray signatures from material originating from differing depths in the targets, thus providing a record of the spatial structure of the ablation front as it progressed through the signature material.

The placement and orientation of the various diagnostics are shown from the top view in Fig. 1. The lines of sight of the target chamber diagnostics all lay in the equatorial plane of the chamber. The laser entered the chamber at an angle of 35.5° with respect to this plane. The x-ray emission from the target was captured by a pinhole camera (XPC) of resolution 10 μm and a Bragg-crystal spectrometer (XCS). Both the XPC and XCS used Kodak DEF film as the recording medium and both instruments featured a beryllium entrance window that provided an energy cutoff at 1 keV. The filter effectively attenuated the emission originating from the CH plasma while transmitting a large fraction of the signature emission. The XCS incorporated a TlAP crystal that Bragg reflected the x rays over the range 5–12 Å, allowing the K-shell emission lines of the highly stripped Al and Na ions to be recorded. The relative strengths of the heliumlike and hydrogenlike lines provide a temperature sensitive diagnostic above 300 and 200 eV for the species Al and Na, respectively. A 35-μm-wide entrance slit provided spatial resolution of the emission along one direction. Due to the limitations imposed by the port configuration of the target chamber it was not possible for both instruments to concurrently resolve along the direction of the modulations. Consequently, the orientation of the beam mask was alternated throughout the experiments to provide XPC- or XCS-resolved records of the modulated x-ray structure. Throughout the course of the x-ray experiments, the laser energy on target was recorded by diverting a fraction of the beam to a volume absorbing calorim-

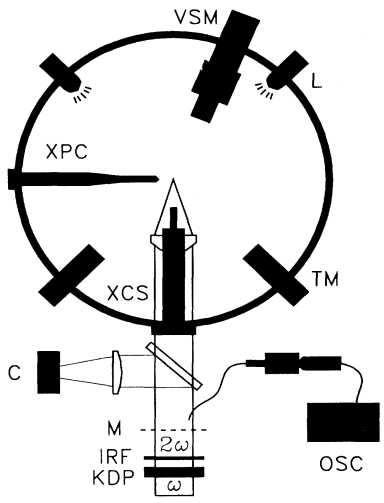

FIG. 1. Top view of the target chamber and diagnostics, which included a Bragg crystal spectrometer (XCS), x-ray pinhole camera (XPC), visible Schwarzschild microscope (VSM), and optical streak camera (OSC). After the laser beam was frequency doubled using a KDP crystal and infrared filter (IRF), a fraction of the light was diverged to an energy calorimeter (C). A mask (M) was inserted into the beam when spatial modulations were required. Back-lighting halogen lamps (L) and target monitors (TM) enabled accurate positioning of the focal spot and target.

eter. The temporal profile of the laser was captured by 150 cm of optical fiber and relayed to a Hamamatsu C979 streak camera.

In addition to these diagnostics a visible Schwarzschild microscope [16] (VSM) was used to characterize the focal spot in the independent series of measurements described in Sec. III. The instrumental resolution of 3 μm in the visible was determined by the Rayleigh criterion applied to the acceptance angle of the instrument. The instrument imaged visible light onto Kodak 3200 black and white film. A calibration of this film was performed by exposing samples through a green filter and neutral density step wedge.

III. CHARACTERIZATION OF THE FOCAL SPOT

Prior to the x-ray experiments, measurements were taken to characterize the intensity distribution on target for both focal conditions, to be used as input parameters for the simulations. It was also desirable to verify, for the case of the spatially modulated beam, the spatial period of the intensity modulations on target and the amount of diffracted light that could be expected to fall in the low-intensity or "shadow" regions of the target. For the case of the tight focus condition, the intensity levels that could be expected outside the nominal focal spot radius were estimated. Since imperfections in the individual components of the optical system could influence these issues, the measurements were conducted using the same optical path as that used in the transport experiments. A set of coparallel glass neutral density filters were inserted into the beam to attenuate the energy by a factor of 10^5 while preserving the intensity profile of the beam at the focusing lens.

The laser was focused nondestructively onto a target and a small fraction of the forward scattered light was imaged by the VSM onto film. Spatial calibration for the measurements was obtained by imaging scattered helium neon laser light from a precision mesh target positioned at the focus. The scattering target used in the focal spot measurements consisted of semitransparent adhesive tape, which was treated with toluene to remove the adhesive layer; the resulting target thickness was 45 μm. Densitometer measurements verified that only a small fraction of collimated light incident on the target was scattered into the collecting solid angle of the VSM and, consequently, that loss of resolution due to scattering within the target was not an issue. An estimate of the spatial resolution of the scattering measurement was made by imaging backlit pinhole apertures onto film using a microscope and comparing the sizes of images produced from apertures covered with tape to those uncovered. Based on these observations, the spatial resolution of the focal spot measurement was somewhat degraded from the VSM resolving limit of 3 μm, but still better than 10 μm.

The first VSM images were acquired using a beam unmodulated by masks. By adjusting the axial position of the focusing lens incrementally, intensity patterns were recorded for a number of positions in the vicinity of the beam waist. A VSM image of the focal spot at the beam waist, with a lineout taken through the center of the image and converted to relative intensity, is shown in Fig. 2. Over 90% of the laser energy was deposited in a ring of inner and outer radii 30 and 60 μm, respectively. Beyond the outer radius, circular diffraction rings could be observed. However, based on the film calibration, the intensity beyond the 60 μm radius is less than 1% of the average intensity in the ring. Despite the strong azimuthal structure evident in the intensity pattern, it possessed a well defined spot radius and was therefore deemed suitable for the lateral transport studies.

For the case of modulated intensity experiments the choice of the focal condition was dictated by the spatial resolution of the instruments and the requirement that the target plane be sufficiently into the far field to reproduce the strip pattern faithfully. On the diverging side of the beam waist, the beam was deemed unsuitable as it was observed to break up into hot spots. On the converging side of the beam waist, the radial profile exhibited a ring structure consistent with the flat top beam of GEKKO IV. At this axial position the aximuthal variations in the beam intensity could still fluctuate by a factor of 2, due to spatial energy beam imbalance and imperfections in the optics. For this reason, a corresponding asymmetry was often observed in the x-ray emission profiles obtained from the transport experiments. At the focal setting of 312 μm from the beam waist chosen for

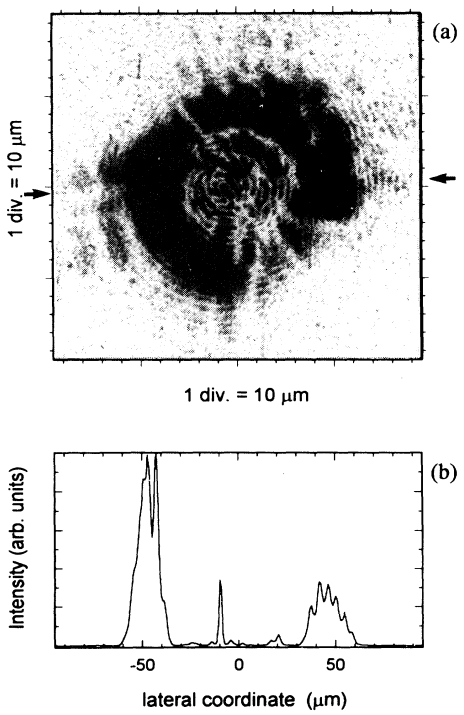

FIG. 2. (a) Visible Schwarzschild microscope image of the tight focus energy distribution exhibits a well-defined radius and azimuthal structure. (b) A lineout taken through the center of the image and along the direction indicated by the arrows, and converted to relative energy, is plotted against source plane coordinates.

these experiments, the beam mask resulted in a spatial modulation of 112 μm being imposed on the intensity envelope on target. The modulations were not perfectly sharp edged, but exhibited some diffraction into the shadow regions. From converted densitometer scans taken across the modulation, it was estimated that the fraction of diffracted light into the shadow regions did not exceed 10% of that in the irradiated regions.

To provide an independent verification of the scattering measurements, a microablation study was undertaken that involved taking low-energy shots on aluminum targets coated with 100 Å of gold. The targets were then removed from the chamber and photographed under a microscope. By identifying those areas of the targets from which the gold layer had completely ablated under a number of incident energies, an intensity profile for the beam could be reconstructed. The resulting estimates for the spatial periodicity of the modulations and the fraction of diffracted light were found to be in good agreement with the VSM measurements.

IV. EXPERIMENTAL RESULTS

X-ray data were acquired under modulated intensity conditions from single-signature targets irradiated by laser pluses of 860 ps. The data acquired under the tight focus setting were collected from double-layer targets at the shorter pulse setting. Representative pinhole images for the two focal conditions are shown in Fig. 3. Image (a) was obtained from single tracer targets irradiated by the spatially modulated beam and image (c) from a double tracer irradiated under tight focus conditions. The position of the laser beam is marked by dashed lines. The peak intensities and CH overcoat depths for these shots were (a) 3.3×10^{13} W/cm^2, 0.54 μm and (c) 2.3×10^{14} W/cm^2, 0.1 μm.

In all cases the pinhole images were dominated by the coronal expansion plumes originating from the directly irradiated regions of the target. Estimates of the density scale lengths of these expansions were made from densitometer scans taken along a direction normal to the target and through the centers of the irradiated regions and converted to photon flux using published measurements for the DEF film response [17]. The shapes of the resulting profiles, which were relatively insensitive to the precise shape of the emission spectra over the collecting bandwidth of the instrument, were assumed to reflect the profiles of the electron density squared, since the collisional and cascade decay rates that determine the line and continuum emission scale as this parameter. The profiles were fit to curves of the form $\exp(-2x/L)$, where L is the characteristic density scale length of the plasma, yielding characteristic density scale lengths for the highest energy shots of 100 μm for the 860-ps shots. In the tight focus conditions scale lengths of up to 50 μm were inferred.

In Fig. 3(a) one may observe x-ray emission adjacent to the target surface between the expansion plumes. A lateral densitometer lineout from the image, taken through direction indicated by the arrows in (a), is shown in (b). This emission is indicative of lateral heating and ablation in the nonirradiated or shadow region of the target. For this shot, which corresponds to the maximum intensity in the modulated beam focal condition a minimum ablated areal density of 0.59–0.86 g cm^{-3} μm in the shadow regions is indicated. The lateral emission was not as visually prominent in images from shots of less energy. However, lateral densitometer lineouts from these images also indicate x-ray levels of about 10% of those in the irradiated regions for all of the targets. We estimated an upper limit on the heating of the shadow region by diffracted light, assuming the maximum intensity incident there was 10% of that incident on the irradiated regions. Measured electron temperatures (see below) were assumed to characterize the plasma expanding from the irradiated regions and intensity scaling predicted by one-dimensional (1D) models [2,6] were used to estimate electron temperatures expected in the shadow region if no lateral energy transport occurred. Using these temperatures the x-ray emissivity of the lateral substrate could then be estimated and compared to that of the irradiated region. We find that the recorded x-ray emission levels from the lateral region would then be less than 1% of those recorded from the irradiated regions, once the instrumental filtering was taken into account. We conclude that the diffracted light levels alone cannot account for the observed x-ray levels. However, there was clearly insufficient energy transported into the lateral substrate

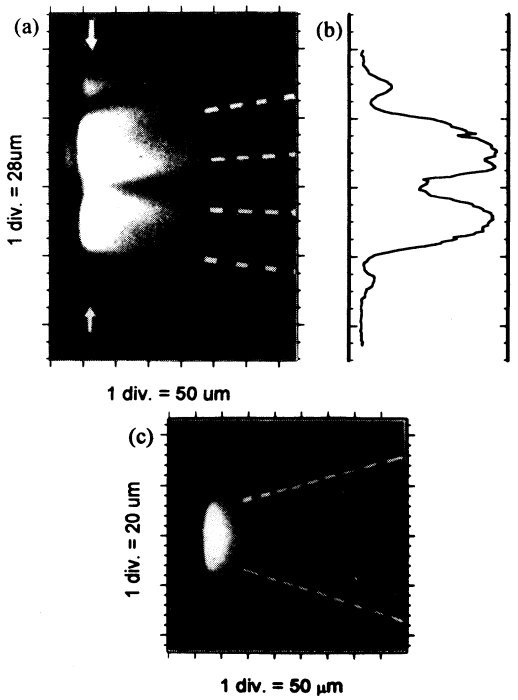

FIG. 3. Representative x-ray pinhole images for the (a) modulated-beam and (c) tight focus conditions. The peak laser intensities and CH overcoat depths were (a) 3.3×10^{13} W/cm^2, 0.54 μm and (c) 2.3×10^{14} W/cm^2, 0.1 μm. The position of the laser beam is shown with dashed lines. (b) A densitometer lineout taken along the lateral direction indicated by the arrows in (a).

to create uniform ablation conditions across the modulation. The width of the bright expansion plumes near the ablation surface did not exceed the nominal 56 μm by more than 10 μm. This value is in accordance with the maximum spatial distance for which significant thermal smoothing is predicted to occur, based on the 1D models of Ref. [1].

For the case of tight focus conditions, observation of x-ray emission beyond the focal spot was limited to targets of overcoat 0.1 μm or less, from which emission levels not exceeding 10% of those from the focal region were recorded out to a radius of 100 μm. Despite the higher intensities prevalent in the tight focus shots, there was no recordable evidence of x-ray emission from the substrate beyond this radius.

The XCS data generally supported that of the pinhole diagnostic. Representative spectra obtained by this spectrometer are shown in Fig. 4 for the two spatial beam profiles and target types. The data of Fig. 4(a) were recorded from a target with a single Al layer and 0.24-μm overcoat irradiated by a modulated beam of peak intensity 2.3×10^{13} W/cm^2; the data of Fig. 4(b) were recorded from an uncoated double-signature target irradiated by the tight focus beam of peak intensity 2.0×10^{14} W/cm^2.

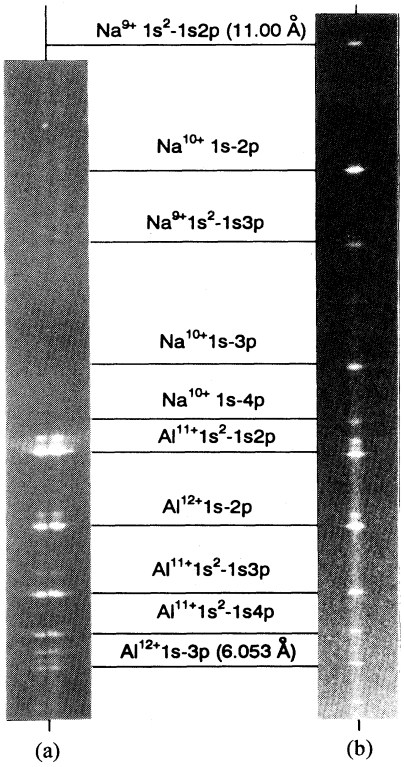

FIG. 4. Representative x-ray spectrometer images for the (a) modulated-beam and (b) tight focus conditions. The spectra were dominated by the *K*-shell lines identified in the figure. The spectrum (a) was recorded from a single-signature target with a CH overcoat thickness of 0.24 μm irradiated at a peak intensity of 2.3×10^{13} W/cm^2; the spectrum (b) was recorded from an uncoated double-signature target irradiated at a peak intensity of 2.0×10^{14} W/cm^2.

The dominant emission features are the *K*-shell emission lines from the Al^{11+} and Na^{9+} ($1s^2$-$1snp$) and Al^{12+} and Na^{10+} ($1s$-np) series and their satellites. Densitometer wavelength scans of the data were converted to spectra using published film and filter response functions [18]. Theoretical spectra generated by the RATION code [19] were fit to the experimental spectra to obtain temperature estimates for the signature layers. The spectra were well modeled under the steady state assumption of RATION, except in the case of uncoated targets, for which evidence of recombination was observed [20]. These data were not included in the present analysis. Electron temperatures fell within the range 300–600 eV for the case of the modulated intensity shots and 300–700 eV for the tight focus shots. Estimates for particular shots were found to fall between theoretical values obtained from 1D isothermal [2] and self-regulating models [6].

In order to assess the effect of energy transport into the shadow regions of the target, lateral densitometer scans of the resonance lines were converted to intensity profiles and deconvolved from the instrumental slit function by using an algorithm described by Jones, Venkataraghavan, and Hopkins [21]. The sampling aperture of the densitometer was kept small in order to minimize the effect of the dependence of the instrumental source function along the scanning direction. Lateral profiles of the Al^{12+} $1s$-$2p$ and Al^{11+} $1s^2$-$1s2p$ (singlet) line emission, obtained from Fig. 4(a), are shown in Fig. 5. These profiles are representative, exhibiting two prominent emission features originating from the irradiated regions and indicating limited emission originating from the shadow regions. The average *e*-folding widths from the two prominences were averaged for each profile and plotted as a function of the areal density of the CH overcoats of the targets. Discrepancies between the two *e*-folding values obtained

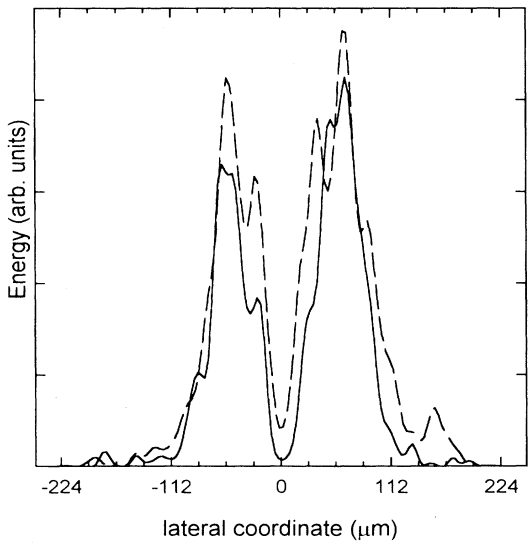

FIG. 5. Typical lateral emission profiles for the Al^{2+} (solid) and Al^{11+} (dashed) resonance lines as recorded with the crystal spectrometer. The laser intensity and pulse width were 2.3×10^{13} W/cm^2 and 860 ps.

from any given profile could be attributed to spatial energy imbalance in the laser beam. These discrepancies were incorporated into the error bars. A minimum of 7% error due to target positioning uncertainty was also assumed for each point.

Results for the aluminum resonance lines are summarized in Fig. 6. The plots give little indication that the ablation front extends beyond the nominal 56 μm widths of the irradiated strips. The Al^{2+} emission originated chiefly from within these regions. The Al^{11+} emission profiles exhibit a moderate widening for low overcoat areal densities, possibly indicating lateral heating of the tracer to temperatures below 400 eV, for which fractional populations of the Al^{12+} states are expected to be very low.

In the case of tight focus shots, the emission above 1 keV recorded by the XCS was again found to be essentially confined to the focal spot region. Lateral densitometer scans were again taken across the brightest emission lines of each spectrum and converted to relative intensity using the filter transmission, film response, and crystal reflectivity curves. Lateral profiles obtained from three shots of peak laser intensity 2.0×10^{14} W/cm^2 are shown in Fig. 7. The overcoat depths of the targets were (a) 0, (b) 0.1, and (c) 0.9 μm, respectively. In all figures the emission levels beyond the focal spot radius of 55 μm are less than 20% of the peak value. Intensity levels above 10% of peak in the lateral region were observed only from targets with overcoating of less than 0.1 μm. In accord with the XPC images, no significant levels of line emission were recorded beyond a 100 μm radius for any of the data. The emission curves originating from the more deeply buried Al layer are invariably narrower than those of the Na emission. Moreover, as the overcoat thickness is increased the widths of the profiles are confined within the nominal radius of the focal spot.

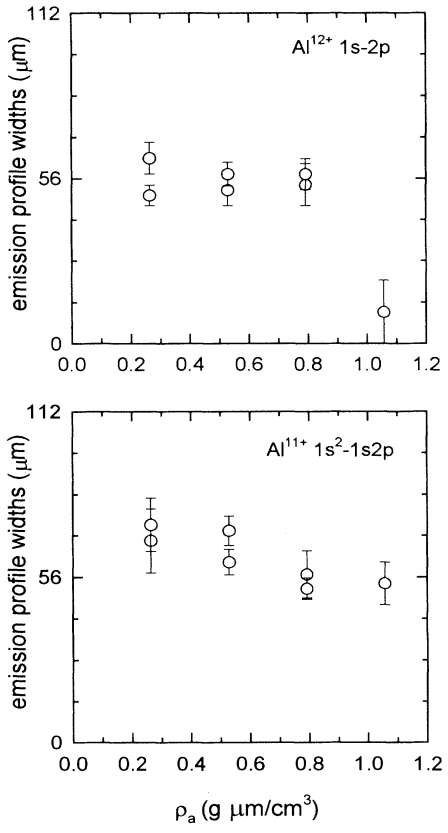

FIG. 6. Lateral widths of the emission profiles of two K-shell resonance lines for the 860-ps laser pulse data. The data are plotted as a function of the areal density of the overcoat layer.

V. SIMULATION RESULTS

In this section we present the predictions of two simulations that were performed using the 2D single-fluid hydrodynamic code IZANAMI. This code is based on an improved particle-in-a-cell implementation of the Navier-Stokes equations that exhibits second-order accuracy in advection [22] and incorporates an average ion model for

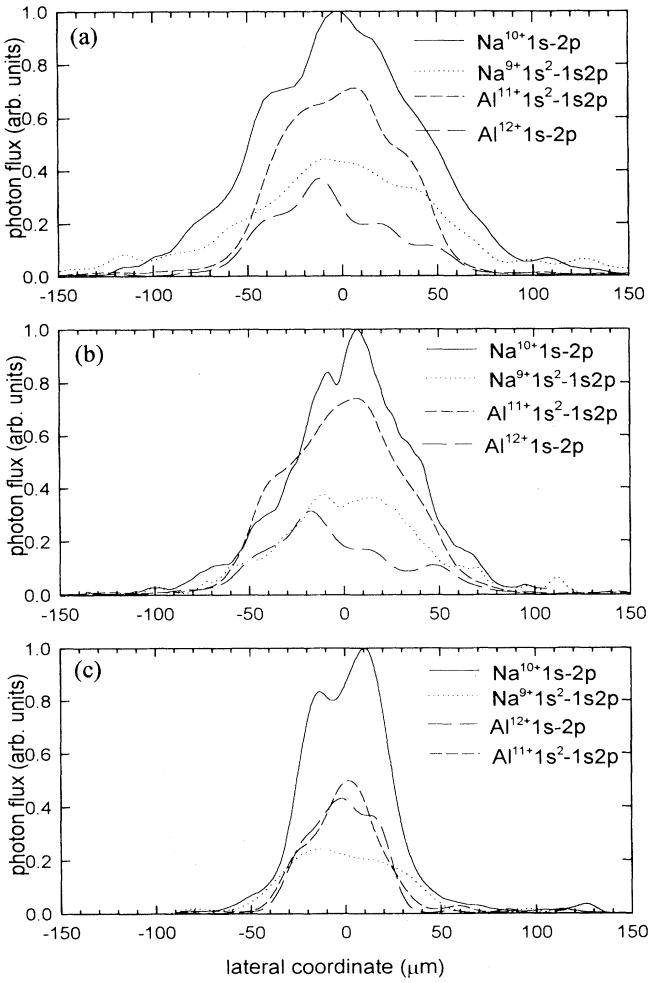

FIG. 7. Lateral profiles of K-shell lines recorded from double tracer targets with CH overcoats of (a) 0.0, (b) 0.1, and (c) 0.9 μm irradiated by 400-ps laser pluses of peak intensity 2×10^{14} W/cm^2. The profiles exhibit progressive narrowing with increasing overcoat depth.

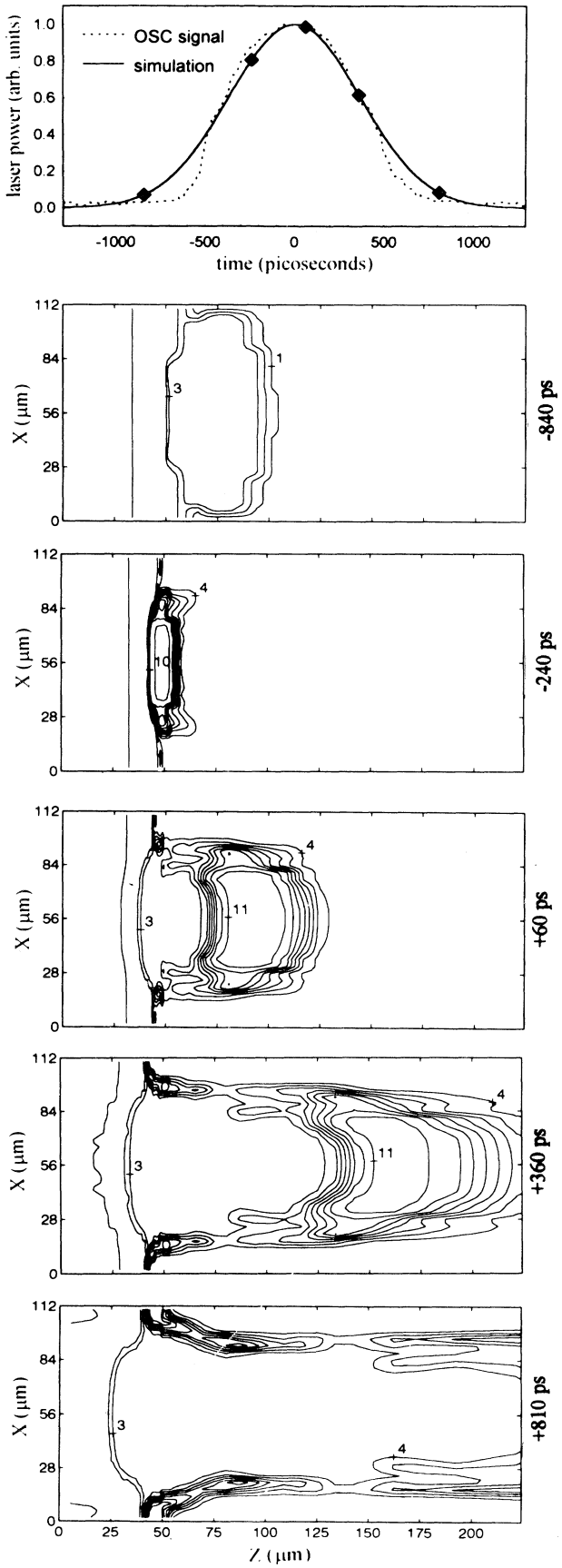

the atomic physics [23]. A multigroup diffusion model for radiation transport is used in IZANAMI. In order to model thermal conduction, a classical flux-limited Spitzer-Harm treatment is adopted. In addition, the generation and evolution of magnetic field structure and its inhibiting effect on electron thermal transport is also included, following the treatment by Braginskii [24]. For the simulations discussed herein, a flux limiter of 0.1 was imposed on the thermal transport along both spatial directions. This value has proved successful in modeling a number of experiments performed at Osaka using 0.53-μm lasers [25]. The code was capable of handling several different macroparticle species, thus allowing the modeling of the multilayer targets used in the experiments. The simulation runs were executed on an NEC supercomputer, with 10^6 particles loaded at the beginning of the simulation.

The first simulation was designed to model the beam-target interaction of the target shot of Fig. 3(a), with CH and aluminum fluid particles initially distributed in a CH|Al|CH sandwich of layer thicknesses 0.54|0.1|15 μm. The simulations were run on a nonuniform Cartesian Eulerian grid of (69 axial cells) $\times$ (30 lateral cells) with corresponding axial (z) and lateral (x) domain dimensions of 730 and 112 μm. A reflective boundary condition was applied at the boundaries parallel to the laser axis. Fluid particles reaching these boundaries were reflected with momentum change $P_x \rightarrow -P_x$, $P_z \rightarrow P_z$. The spatial profile of the laser was a step function deposited in the central 56 μm of the domain. The temporal laser pulse was a Gaussian ($\Delta_{\mathrm{FWHM}} = 860$ ps) and was switched on at $t = -1.5\Delta_{\mathrm{FWHM}} = -1290$ ps, where the temporal origin has been defined at the peak of the pulse. The peak incident laser intensity was 3.3×10^{13} W/cm^2. The laser absorption mechanism was assumed to be inverse bremsstrahlung, with 100% reflection assumed at the critical surface. Effects due to beam refraction were not included in the present simulation.

The history of the ablation process for the first simulation is illustrated in the series of contour plots of the average ionization $\bar{Z}$ in Fig. 8. The temporal profile of the laser pulse and the simulation times for the contour plots, namely, $t = -840$, -240, $+60$, $+360$, and $+810$ ps, are shown in the top graph. Also included is the profile of a typical experimental laser pulse as recorded by the optical streak camera. In the contour plots the laser propagates from the right within the central 56 μm of the simulation grid.

In the first contour plot the laterally expanding plasma has just reached the lateral boundaries of the simulation. The expansion results in axial density profiles that exhibit

FIG. 8. Ionization contours predicted by an IZANAMI simulation of a single-signature-layer target irradiated by a modulated laser beam. The temporal shape of the simulation laser pulse is plotted in the uppermost frame (solid line), along with a typical experimental pulse (dashed line). The remaining plots show the average ionization at the instants indicated by diamonds in the upper plot.

moderate variation in the lateral direction throughout the remainder of the pulse. In the case of the real laser-target interaction the presence of such density profiles in the shadow region would ensure that low-level diffracted laser light is effectly absorbed before reaching the vicinity of the target. The contour $\bar{Z}=4$ may be interpreted as the boundary between the aluminum and CH, which is essentially fully ionized to $\bar{Z}=3.5$ in the corona. The tracer begins to ablate at about -300 ps and has finished by the time of the third plot ($+60$ ps). The simulation predicts that there is sufficient lateral transport of energy to ablate away the tracer in the shadow region during the falling phase of the laser pulse. The last of this tracer is ablating at $t=+810$ ps. By way of comparison, in another simulation run under identical laser conditions but with a target of 0.12-μm overcoat, ablation of the lateral tracer had completed by 100 ps after the peak of the pulse. The areal density of material removed from the target in the irradiated and shadow region were about 1.6 and 1.1 g cm^{-2} μm, respectively.

In the present simulation the average ionization state of the lateral tracer was less than 9 and the electron temperature less than 300 eV. Such conditions imply low population levels in the highest ionization states of Al, which is consistent with the absence of observed Al^{12+} K-shell emission from the lateral region. X-ray emissivity spectra generated by the IZANAMI atomic physics routines were convolved with the XPC filter response function and integrated over energy and time to produce the spatial emissivity pattern shown in Fig. 9. Emission from the lateral Al tracer moderately enhances the x-ray flux from the shadow region, at levels of about 10% of those from the irradiated region, in qualitative agreement with the XPC images.

The spatial characteristics of the energy transport were determined by a balance between laser absorption, advection, and electron thermal conduction mechanisms. Figure 10 shows the magnitude (W/cm^2) and direction (arrows) of the thermal flux in the vicinity of the target surface and lower half-domain at $t=60$ ps. Contours of n_c and $10n_c$ are also indicated with dotted lines. At $t=60$ ps most of the laser absorption occurs in the region 10–60 μm downstream from the critical surface. The

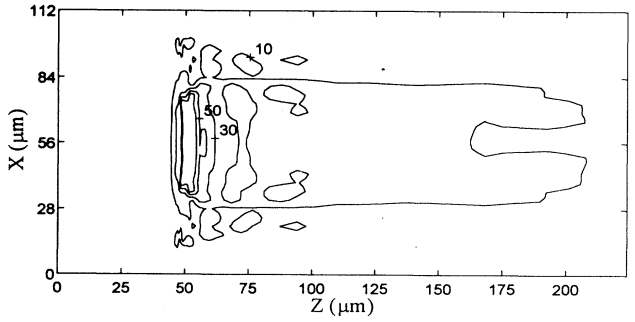

FIG. 9. Time- and wavelength-integrated x-ray emissivity pattern predicted by the average ion model for the IZANAMI simulation of Fig. 8. The effect of the XPC filter response was included in the calculation.

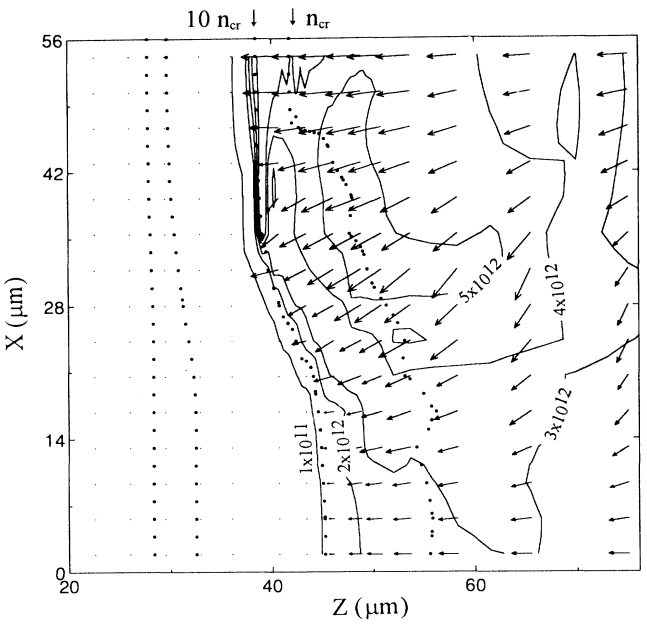

FIG. 10. Thermal flux in the vicinity of the target at $t=+60$ ps for the IZANAMI simulation of Fig. 8. Half of the lateral domain is shown, with the laser absorption region in the top half of the plot. The magnitude of the flux in W/cm^2 is shown by the contours and the direction of the heat flow is indicated by arrows. Contours of n_c and $10n_c$ are indicated by dashed lines.

thermal energy is transported axially and laterally from this region toward the target along rather moderate temperature gradients and against the hydrodynamic flow. A significant amount of axially directed heat transport does occur in the shadow regions of the target, facilitated by the lateral advection of plasma, which creates a thermal bath adjacent to the lateral substrate. This region of inward transport is characterized by electron temperatures below 300 eV and an axial energy flux below 10^{12} W/cm^3.

The magnetic fields were predicted to have a very limited effect on the lateral ablation process. The fields generated by the $\nabla n \times \nabla T$ effect at the boundary between the irradiated and shadow regions reached peak values of 7×10^5 G early in the simulation. These field strengths were not sufficiently strong to seriously affect transport near the target surface. The imposed flux limit of 0.1 influenced transport in this ablation region more strongly, typically reducing the Spitzer-Harm conductivity by a factor of ~ 2. The magnetic fields induced considerable heat flow inhibition in the underdense corona, but in this region the outward plasma expansion effectively decoupled the thermal transport from the target.

A second IZANAMI simulation was run to model the conditions of a tight focus, 6.6-J, 400-ps FWHM laser shot on an uncoated double-tracer target. This simulation was run on a cylindrical Eulerian mesh system of axial and radial dimensions 616×150 μm,^{2} with a reflective boundary condition applied at the laser axis and a free boundary condition (allowing the escape of macroparticles and energy from the simulation domain) at the outer

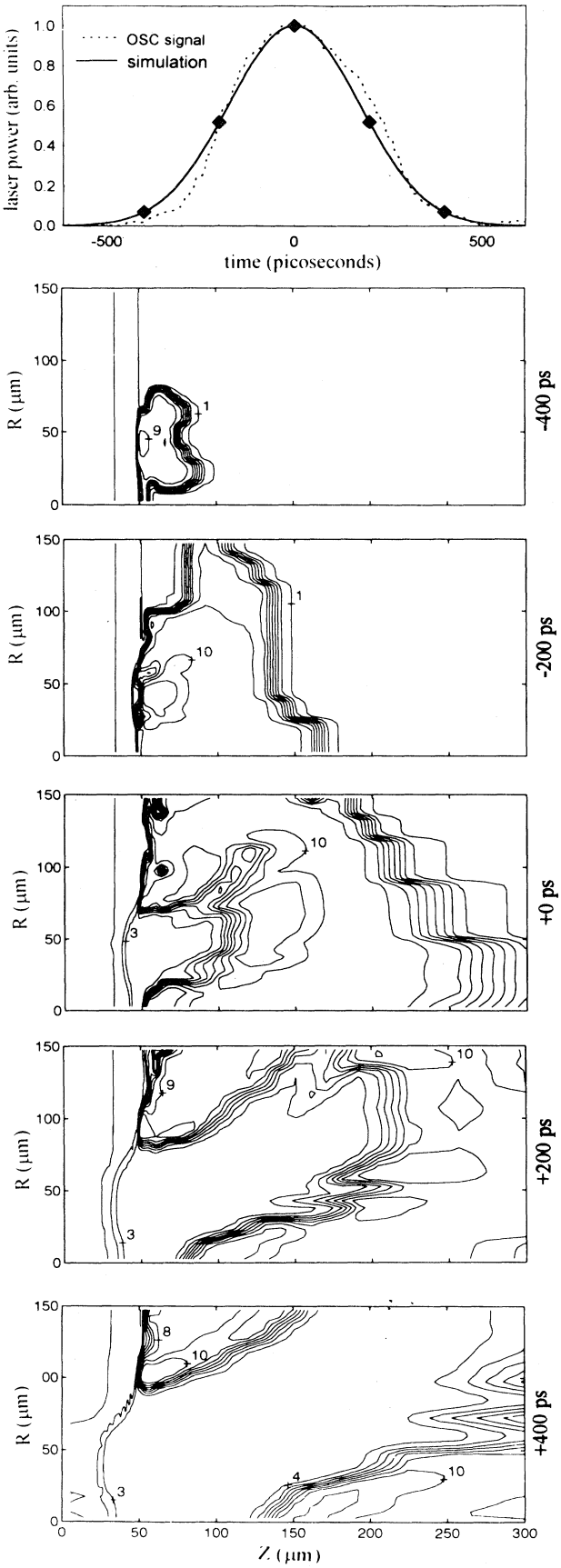

radius of the simulation. Three species of fluid particles were distributed so as to simulate a NaF|Al|CH multilayer target with corresponding layer thicknesses of 0.1|0.1|15 μm, from which the widest K-shell line emission profiles were observed. The focal intensity pattern was approximated by a high-intensity annulus (inner radius 30 μm, outer radius 55 μm) superimposed on a low-intensity disk (radius 55 μm), such that the intensity of the high-intensity region was ten times that in the central region. The peak incident intensity reached in the annular region was 2.2×10^{14} W/cm^2.

Predictions for the ionization history are illustrated in Fig. 11. The simulation pulse and a typical experimental streak camera trace are again shown in the upper plot of the figure. Contours are plotted for $t=-400$, -200, 0, $+200$, and $+400$ ps, with $t=0$ again representing the temporal peak of the laser pulse. The lower horizontal axis represents the central axis and the laser propagates from right to left. The hydrodynamic flow exhibits a strong radial component throughout the simulation. Thermal transport into the lateral region of the target creates a high-density plasma that expands radially outward along the target surface. Relatively isothermal conditions prevail in this laterally extended region throughout the laser pulse, with electron temperature peaking above 800 eV. Since fully ionized NaF has an average ionization of 10, this contour value may be used to estimate the position of the boundary between the NaF and Al tracer material, while the $Z=4$ contour may be interpreted as CH-tracer boundary. Both tracer layers have ablated through in the high-intensity annulus by the time of the peak of the pulse. Within the focal spot the final ablation depth is approximately 1.5 μm. The ablation depth decreases in a roughly linear fashion with radius from $R=60$ to 110 μm, beyond which little material ablates. Approximately 50% of the final ablated mass therefore originates from beyond the lateral regions. The contour and quiver plots of Fig. 12 display the thermal flux at $t=0$ ps. Thermal transport may be seen to play an important role well beyond the spot radius.

Magnetic fields are generated predominantly by the $\nabla n\times\nabla T$ effect at the edge of the spot and at the boundary between the low- and high-intensity regions of the laser beam. Although the resulting toroidal structures grow to peak values of several megagauss and strongly inhibit the local thermal transport, they were found to have limited effect on the overall energy balance. This is thought to be due to the localized region of inhibition (with characteristic scale of ~20 μm) and the motion of the local field maxima, which expanded from the edge of the focus, following the edge of plasma expansion where

FIG. 11. Ionization contours predicted by an IZANAMI simulation of an uncoated double-signature-layer target irradiated by a tight focus laser beam. The temporal shape of the simulation laser pulse is plotted in the uppermost frame (solid line), along with a typical experimental pulse (dashed line). The remaining plots show the average ionization at the instants indicated by diamonds in the upper plot.

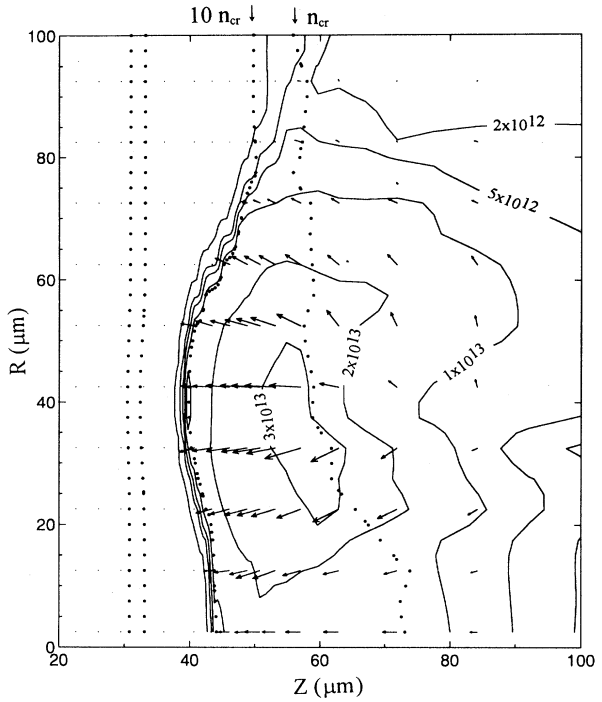

FIG. 12. Magnitude (contours) and direction (arrows) of the thermal energy flux at the peak of the pulse for the IZANAMI simulation of Fig. 11. The contour units are W/cm^2. Contours of n_c and $10n_c$ are indicated by dashed lines.

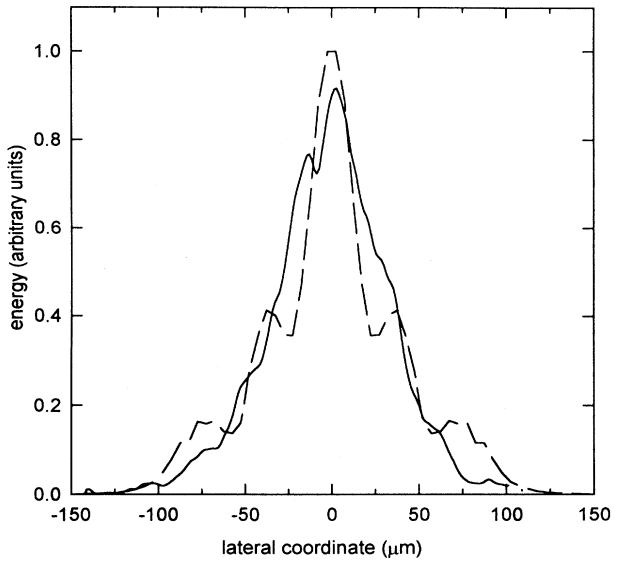

FIG. 13. Spatial profile of the Na^{10+} 1*s*-2*p* line from the uppermost plot of Fig. 8 (solid line) is overlaid with a spatial profile (dashed line) calculated using the *K*-shell line emissivity generated by the IZANAMI simulation of Fig. 11.

the $\nabla n \times \nabla T$ term was highest.

In Fig. 13 the experimental lateral profile of the Na^{11+} 1*s*-2*p* line (solid curve) is superimposed on a theoretical profile generated by transport calculations done along the line of sight of the XCS (dashed curve). The total tracer *K*-shell line emissivity predicted by the atomic physics package of IZANAMI was used to generate a sequence of emission profiles at simulation intervals of 100 ps. In generating the profiles, account was taken of the effective instrumental source function contributing to the recorded densitometer scan, based upon the plasma size and the published dispersion properties of the TIAP crystal [18]. The sequence of curves was then time integrated to produce the final profile. Both profiles have been normalized with respect to the laterally integrated signal. Fairly good agreement is achieved with respect to the overall shape of the profiles.

VI. CONCLUSIONS

Lateral x-ray emission structure from multilayer solid targets irradiated under two focal spot conditions were studied and compared with the predictions of a 2D hydrodynamic code with heat conductivity corrected for self-generated magnetic fields and axial and lateral thermal flux limiters set to 0.1. Experimentally observed fractional emission levels on the order of 10% were observed from the lateral substrate. Such emission levels were indicative of lateral energy transport, although the experiments did not allow us to set any definitive limits to the lateral flux. Good agreement was demonstrated between the spatial structure of the x-ray emission as predicted by the IZANAMI code and the data, under the assumption that lateral energy transport into the substrate was determined mainly by the mechanisms of advection and classical flux-limited electron thermal transport. A significant fraction of the final ablated mass may originate from the nonirradiated substrate. However, the energy flux into this material was insufficient to heat it to the temperatures that would result in x-ray emission levels comparable to those of the irradiated regions.

ACKNOWLEDGMENTS

The authors wish to thank H. Sugio, T. Hagihara, and T. Sakamoto for technical assistance in the operation of GEKKO IV and M. Takagi for help in fabrication of the targets. This work was funded jointly by the Japanese Ministry of Education, the International Communications Foundation, and the Natural Science and Engineering Research Council of Canada.

[1] J. H. Gardner and S. E. Bodner, Phys. Rev. Lett. **47**, 1137 (1981).
[2] W. M. Manheimer, D. G. Colombant, and J. H. Gardner, Phys. Fluids **25**, 1644 (1982).
[3] S. P. Obenschain, R. H. Lehmberg, and B. H. Ripin, Appl. Phys. Lett. **37**, 903 (1980); S. P. Obenschain *et al.*, Phys. Rev. Lett. **46**, 1402 (1981).
[4] A. J. Cole *et al.*, J. Phys. D **15**, 1689 (1982).
[5] J. L. Bocher *et al.*, Phys. Rev. Lett. **52**, 823 (1984).
[6] R. Fabbro, C. Max, and E. Fabre, Phys. Fluids **28**, 1463 (1985).
[7] C. L. Shepard and P. M. Campbell, Phys. Rev. A **39**, 1344 (1989).
[8] M. Kado *et al.*, J. Plasma Fusion Res. **70**, 877 (1994).
[9] I. Matsushima *et al.*, J. Appl. Phys. **58**, 1674 (1985).
[10] M. Desselberger *et al.*, Phys. Rev. Lett. **68**, 1539 (1992).
[11] M. H. Key *et al.*, Phys. Fluids **26**, 2011 (1983).
[12] P. D. Gupta *et al.*, Phys. Rev. A **33**, 3531 (1986).
[13] W. C. Mead *et al.*, Phys. Fluids **27**, 1301 (1984).
[14] R. Benattar and J. Godart, Opt. Commun. **51**, 260 (1984); **59**, 272 (1986).
[15] D. S. Montgomery *et al.*, Phys. Rev. Lett. **73**, 2055 (1994).
[16] M. Kado *et al.*, Opt. Lett. **16**, 109 (1991).
[17] B. L. Henke *et al.*, J. Opt. Soc. Am. B **3**, 1540 (1986).
[18] B. L. Henke *et al.*, At. Data Nucl. Data Tables **27**, 1 (1982).
[19] R. W. Lee and B. L. Whitten, J. Quant. Spectrosc. Radiat. Transfer **32**, 91 (1984).
[20] D. Vick *et al.*, Phys. Rev. E **48**, 2308 (1993).
[21] R. N. Jones, R. Venkataraghavan, and J. W. Hopkins, Spectrochim. Acta **23A**, 925 (1967).
[22] A. Nishiguchi and T. Yabe, J. Comput. Phys. **52**, 390 (1983).
[23] M. Itoh, T. Yabe, and S. Kiyokawa, Phys. Rev. A **35**, 233 (1987).
[24] A. Nishiguchi *et al.*, Phys. Rev. Lett. **53**, 262 (1984); S. I. Braginskii, in *Reviews of Plasma Physics* (Consultants Bureau, New York, 1965), Vol. 1.
[25] M. Katayama, A. Nishiguchi, and H. Azechi, J. Plasma Fusion Res. **69**, 1036 (1993); T. Endo *et al.*, Phys. Rev. Lett. **74**, 3608 (1995).

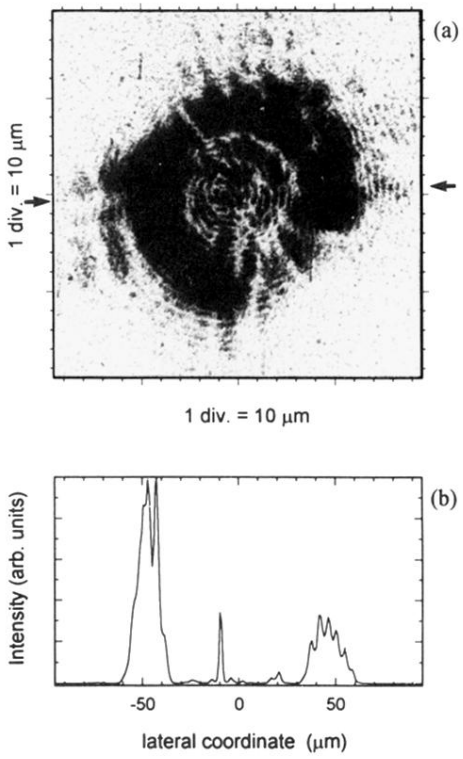

FIG. 2. (a) Visible Schwarzschild microscope image of the tight focus energy distribution exhibits a well-defined radius and azimuthal structure. (b) A lineout taken through the center of the image and along the direction indicated by the arrows, and converted to relative energy, is plotted against source plane coordinates.

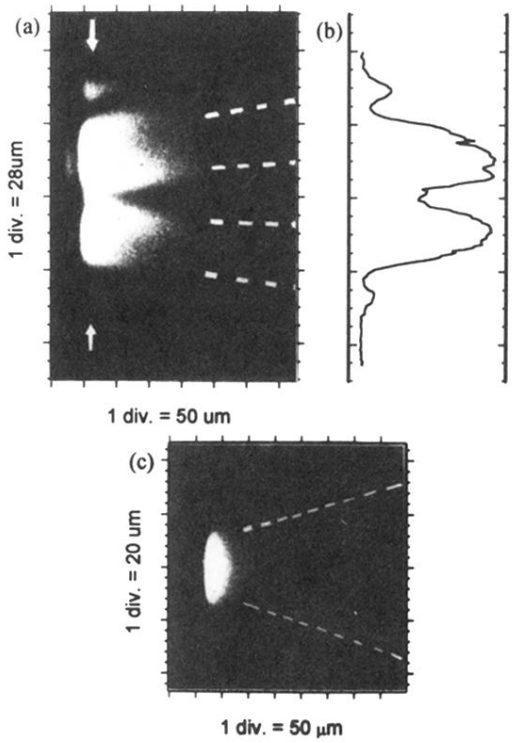

FIG. 3. Representative x-ray pinhole images for the (a) modulated-beam and (c) tight focus conditions. The peak laser intensities and CH overcoat depths were (a) 3.3×10^{13} W/cm^2, 0.54 μm and (c) 2.3×10^{14} W/cm^2, 0.1 μm. The position of the laser beam is shown with dashed lines. (b) A densitometer lineout taken along the lateral direction indicated by the arrows in (a).

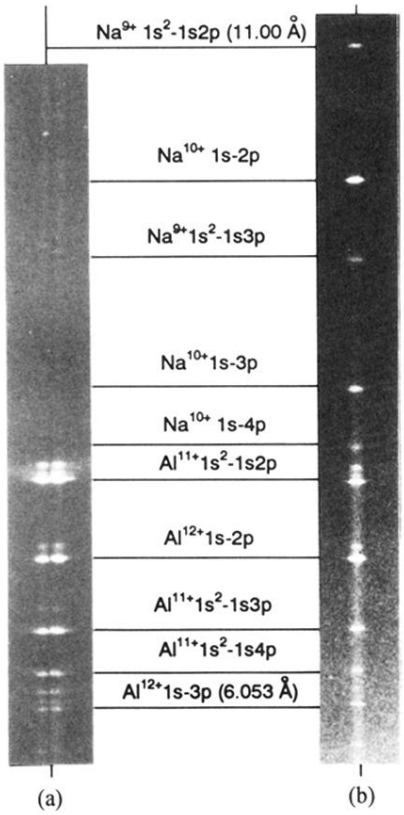

FIG. 4. Representative x-ray spectrometer images for the (a) modulated-beam and (b) tight focus conditions. The spectra were dominated by the K-shell lines identified in the figure. The spectrum (a) was recorded from a single-signature target with a CH overcoat thickness of 0.24 μm irradiated at a peak intensity of 2.3×10^{13} W/cm^2; the spectrum (b) was recorded from an uncoated double-signature target irradiated at a peak intensity of 2.0×10^{14} W/cm^2.